

# Optimizing Electromagnetic Hotspots in Plasmonic Bowtie Nanoantennae

Stephanie Dodson,<sup>†</sup> Mohamed Haggui,<sup>‡</sup> Renaud Bachelot,<sup>‡</sup> Jérôme Plain,<sup>\*,‡</sup> Shuzhou Li,<sup>\*,¶</sup> and Qihua Xiong<sup>\*,†,§</sup>

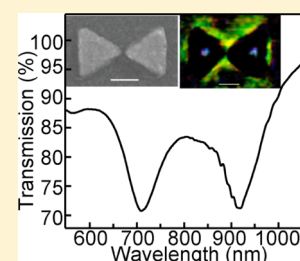
<sup>†</sup>Division of Physics and Applied Physics, School of Physical and Mathematical Sciences, Nanyang Technological University, Singapore 637371

<sup>‡</sup>Laboratoire de Nanotechnologie et d'Instrumentation Optique, ICD, Université de Technologie de Troyes, France

<sup>¶</sup>School of Materials Science and Engineering and <sup>§</sup>Division of Microelectronics, School of Electrical and Electronic Engineering, Nanyang Technological University, Singapore 639798

**ABSTRACT:** Sensitivity is a key factor in the improvement of nanoparticle-based biosensors. Bowtie nanoantennae have shown high sensitivity for both surface-enhanced Raman scattering (SERS)- and localized surface plasmon resonance (LSPR)-based biosensing. In this work, optical bowtie nanoantennae with varying geometries were simulated, fabricated, and characterized. We successfully fabricated sub-5 nm gaps between prisms. The gap between prisms, the prism size, and the radius of curvature of the prism corners were characterized for their effects on the optical and electromagnetic properties. Bowties were characterized using LSPR, SERS, and photochemical near-field imaging. The results indicate that the radius of curvature of the prism corners has an important effect on the SERS abilities of a nanoparticle array. The trends described herein can be utilized to intelligently design highly sensitive SERS and LSPR biosensing substrates.

**SECTION:** Plasmonics, Optical Materials, and Hard Matter



Metallic nanostructures including both chemically synthesized nanoparticles and nanostructures by top-down fabrication have been demonstrated as effective surface-enhanced Raman scattering (SERS) substrates, which can be used toward highly sensitive and specific biosensing.<sup>1</sup> With such high sensitivity SERS biosensors, the earlier diagnosis of diseases, such as cancer, leads to more effective early treatment and higher survival rates. The challenge lies in the fact that the concentration of disease biomarkers at early diagnosis stages is usually very low.<sup>2</sup> This is normally the limiting factor in how early the disease can be detected using proteomic biosensors. Higher detection sensitivity in proteomic biosensors allows for the accurate recognition of lower concentrations of biomarkers, implying the possibility of earlier diagnosis.<sup>2</sup> New, nanotechnology-based biosensors make use of the unique optical and electric properties of nanoscale particles. With this in mind, it is of great interest to exploit the novel properties exhibited by noble metals in the nanoscale for making sensitive, plasmonics-based biosensing technologies. Biosensors based on SERS and localized surface plasmon resonance (LSPR) have great potential as very rapid and sensitive tools.<sup>3,4</sup> SERS biosensing involves the use of enhanced local electric fields of plasmonic devices to increase the Raman signal of biomolecules and biomarkers. These increased signals mean that lower concentrations of biomarkers still produce readable signatures and allow for detection with much lower sample volume or very low concentration samples. LSPR biosensing makes use of the sensitivity of plasmonic devices to their dielectric environment to detect binding events between biomolecules.<sup>5</sup>

A variety of different types of bowtie substrates have been explored for their potential as high sensitivity biosensors. The contours of roughened metal surfaces<sup>6–8</sup> and solution-grown aggregated particles<sup>9,10</sup> were shown to exhibit enhanced Raman signals. Nanosphere lithography fabricated bowties offer good homogeneity and reproducibility but have limited geometries.<sup>11</sup> Structures fabricated using electron beam lithography can be controlled in the nanometer regime for independent variation of geometrical parameters.<sup>12,13</sup> Various geometries of nanoparticles have been explored previously for SERS potential. Particle shape, size, and material will affect the location and intensity of hotspots and the optical and electromagnetic properties of the particle.<sup>14</sup> Experimental work exploring sub-5 nm gaps in other geometries such as spherical dimers has shown great potential for an increased SERS enhancement factor in this regime.<sup>15,16</sup> Spherical, cylindrical, and rectangular prisms were found to be inferior to bowtie nanoantennae prism dimers facing tip to tip for electric field enhancement.<sup>17</sup> Near-field studies making use of photosensitive polymers have been conducted previously on bowtie nanoantennae and hotspots supported by nanorods, and the electric near-field features were well correlated with simulations.<sup>18,19</sup> The gap size between prisms has also been explored previously, and decreasing gap size was found to red shift the resonance.<sup>20,21</sup> The Raman signal increased with decreasing gap size up to the limit of fabrication,

**Received:** December 5, 2012

**Accepted:** January 21, 2013

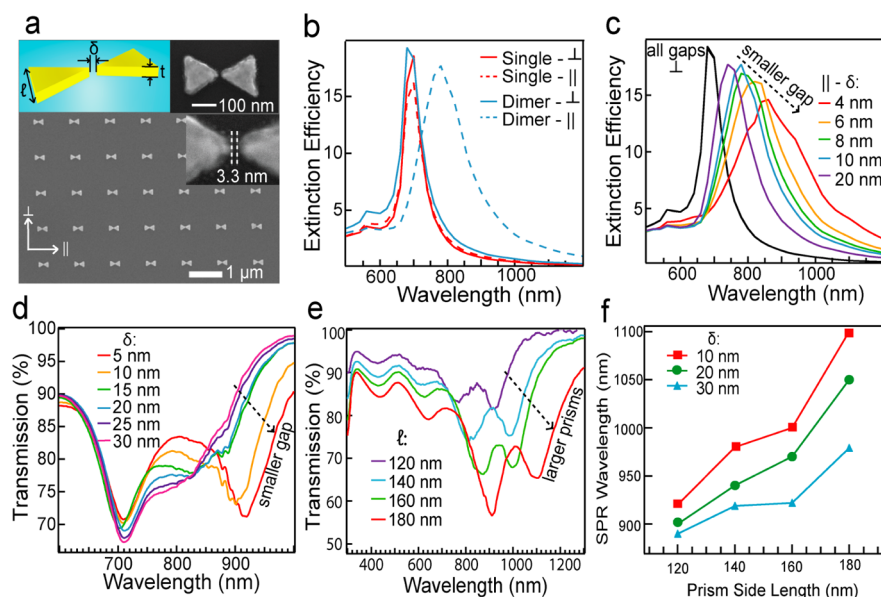


**Figure 1.** LSPR. (a) SEM image of the bowtie nanoantenna array. The left inset shows a diagram illustrating the variable usage used throughout the document. The right insets show high-magnification SEM images of a 3.3 nm gap bowtie nanoantenna. (b) Extinction efficiency of a single prism and prism dimer for both polarizations. (c) Extinction efficiency of prism dimers with varying gap spacing for both polarizations. (d) Transmission spectra of prism dimers with varying gaps between prisms. (e) Transmission spectra of prism dimers with varying prism side lengths. (f) Parallel mode SPR wavelength trends for several gap sizes of bowtie nanoantenna as the prism side length is increased. Calculations were done in DDSCAT.

which previously was an 8 nm gap for a bowtie nanoantenna.<sup>22</sup> Simulations have predicted that the electric field enhancement will continue to increase with decreasing gap size until the range at which quantum effects dominate and the enhancement starts to decrease.<sup>17</sup> Recently, bowtie antenna with gaps in the sub-5 nm regime have been studied for electron energy loss by scanning tunneling electron microscopy.<sup>23</sup> These previous studies inspire great interest in studying bowties with sub-5 nm gaps for potential biosensing applications. The bow angle has been explored for bowtie nanoantennae, and the resonance was found to first blue shift and then red shift with increasing bow angle.<sup>24</sup> To the best of our knowledge, the effect of the radius of curvature (ROC) of the prism corners has not been isolated experimentally and explored.

We show in this work the large-scale, reproducible fabrication of bowtie nanoantennae, systematically exploring how the scattering properties, electric near-field features, and electric field enhancement change as a function of the geometry of the nanoantennae. The bowtie gap size, prism size, thickness, and ROC of the prism corners were explored. Bowtie nanoantennae, shown in Figure 1a, with varying geometric parameters have been fabricated reproducibly in the sub-5 nm regime and characterized. The SPR was characterized by discrete dipole approximation (DDA) scattering calculations and spectroscopy measurements. The electric field was characterized by DDA electric field mapping, Raman spectroscopy, and photochemical near-field imaging.

The LSPR of nanoparticles can be highly controllable and tunable. It was of interest to explore the LSPR of bowtie nanoantennae in order to better understand their optical properties. A highly controllable LSPR also has potential applications in designing sensitive binding event based biosensing platforms. The effect of the gap spacing between the prisms of a bowtie nanoantenna on optical properties was systematically explored by holding all other parameters constant and varying the gap between prisms. A simulation

using the DDA method has been carried out to identify the modes involved in the transmission spectra. As shown in Figure 1b for a bowtie nanoantenna with a size of 150 nm and a gap size 20 nm, when the incoming irradiation polarization is parallel to the bowtie axis, the extinction efficiency has a peak at around 800 nm. When the irradiation polarization is perpendicular to the gap, the peak is at around 700 nm. It should also be noted that the extinction efficiency peaks for both polarizations of a single 150 nm prism are at around 700 nm as well. In Figure 1c, we display the simulation results of the extinction efficiency for a bowtie nanoantenna with the gap spacing,  $\delta$ , varied from 4 to 20 nm when the incoming irradiation is polarized along the gap, keeping the size ( $l = 150$  nm) and thickness ( $t = 30$  nm) constant. Unambiguously, the extinction shows a peak at around 900 nm for a gap size of 4 nm. This peak red shifts significantly as the gap size is decreased from 20 to 4 nm, giving rise to an 800 nm peak for a 20 nm gap. Simulations have also been conducted for the polarization perpendicular to the bowtie axis for different gap sizes. The mode due to polarization perpendicular to the axis of the bowtie did not show a noticeable resonance shift for different gap sizes and was similar to the resonances of single prisms. All of the gaps, 4–20 nm, for perpendicular polarization are shown overlaying each other in black color in Figure 1c.

The modes and effects of the gap on the resonance were studied by taking the transmission spectra of bowtie nanoantennae with gap spacings between 4 and 30 nm, as shown in Figure 1d. Two absorption bands were observed; one band around 700 nm does not vary with the gap spacing, while the other band red shifts as the gap spacing decreases. We observed that both resonance peaks are due to the two different polarization-based modes. In particular, the peak due to longitudinal polarization, parallel to the bowtie axis, shows a systematic red shift with decreasing gap, as suggested by the DDA simulation. The calculated extinction efficiency shows a different resonance for both the polarization parallel to and

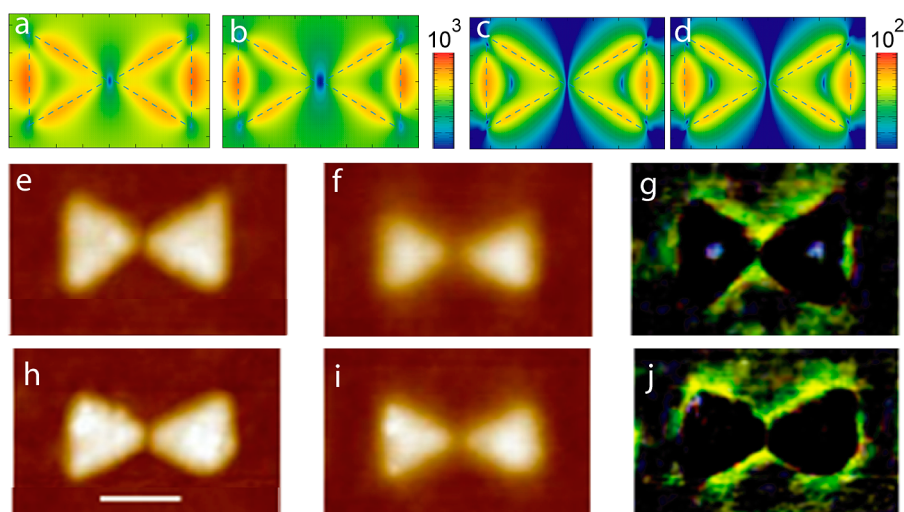


**Figure 2.** Electric near-field. (a–d) Simulated electric near-field of a bowtie nanoantenna with (a,c) a 6 nm gap and (b,d) a 10 nm gap between prisms. (a,b) Simulated total electric near-field,  $|E|^4$ , contour plot. (c,d) Simulated out-of-plane component of electric field,  $|E_z|^2$ , contour plots. (e–j) Experimental near-field imaged using a photosensitive polymer film for (e–g) a 6 nm gap between prisms and (h–j) a 10 nm gap between prisms. (e,h) Atomic force microscopy (AFM) images taken before exposure. (f,i) AFM images taken after exposure. (g,j) Differential images made using image subtraction to view the effect of the near-field. Polarization is longitudinal for all near-field simulated and experimental images.

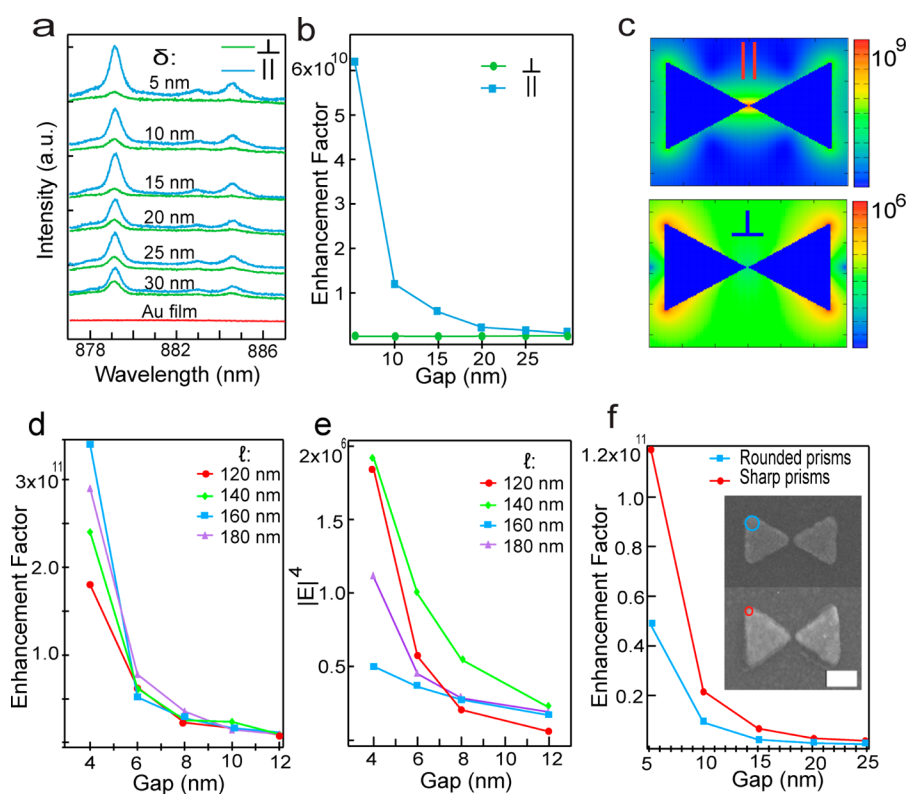


**Figure 3.** SERS. (a) Raman spectra and (b) the enhancement factor of prism dimers with varying gaps between prisms for both polarizations. (c) Simulated electric field contour plot of both modes. (d) Enhancement factor and (e) averaged  $|E|^4$  of prism dimers with varying gaps between prisms and varying prism side lengths. (f) The enhancement factor of prism dimers with varying gaps between prisms for two different ROCs. The inset shows the SEM image of round and sharp prism dimers. The scale bar is 100 nm. Calculations were done using DDSCAT.

perpendicular to the bowtie axis. The peak corresponding to the perpendicular polarization does not vary with changing gap size, while the peak corresponding to the parallel polarization red shifts with decreasing gap size. The transmission data show two peaks, one of which remains constant with a gap change and the other that red shifts with decreasing gap size. The correspondence of the transmission data to the calculated

extinction efficiency implies that the two transmission modes must correspond to the two polarizations. The red shift with decreasing gap size implies a decrease in energy. This well-known behavior is explained by a weakening of the restoring forces for the oscillating electrons due to the presence of the charge distribution of the second particle.<sup>25</sup>



It was of interest to observe the effect of the side length of the prisms of a bowtie nanoantenna on the optical properties. By holding all other parameters constant and varying the side length of prisms, the LSPR has been explored systematically by both simulation and experiments. DDA extinction efficiency simulations were conducted for bowtie nanoantennae with varying prism sizes and gap spacings. Both polarizations, parallel and perpendicular to the bowtie axis, were simulated. The prism size was varied from 120 to 180 nm. The gap spacing was varied from 4 to 10 nm. The SPR for both modes, perpendicular and parallel to the axis, red shifted for increasing prism size. Optical transmission spectra were taken of bowtie nanoantennae with varying prism sizes and gap spacings, as shown in Figure 1e. The prism size was varied from 120 to 180 nm, and the gap size was varied from 4 to 30 nm. The two modes, for polarization perpendicular and parallel to the bowtie axis, red shifted for increasing prism size. The red shift with increasing prism size was more dramatic for smaller gap sizes, as shown in Figure 1f. Both of the modes observed in extinction efficiency simulations red -shifted with increasing prism size. The modes observed in transmission spectroscopy red shifted with increasing prism size, which agreed with simulation.

The visualization of the local near-field is of interest to identify the modes of excitation and to aid in the intelligent design of SERS substrates.<sup>26</sup> Using a photosensitive polymer layer over the bowtie allows the near-field excited in the particle to induce molecular motion and imprint the near-field features into the surface of the polymer. Simulated electric field contour plots were calculated using DDA for 568 nm excitation, as shown in Figure 2a–d. Figure 2a and b shows the simulated total electric near-field,  $|E|^4$ , contour plots for a 6 and 10 nm gap, respectively, with noticeable hotspot features along the edges of the prisms. Figure 2c and d shows the out-of-plane component of electric field,  $|E_z|^2$ , contour plots for a 6 and 10 nm gap, respectively.

Photochemical near-field imaging was used to directly map the near-field of bowtie nanoantennae with 568 nm excitation, as shown in Figure 2e–j. Figure 2e and h shows an AFM image before exposure for a bowtie with 6 and 10 nm gaps between prisms, respectively. After exposure to an external electromagnetic field, the near-field features will have changed the surface of the polymer, as shown in Figure 2f and i for a 6 and 10 nm gap, respectively. In order to better visualize the changes in the polymer surface, differential images were made using image subtraction between the AFM images taken before and after exposure, as shown in Figure 2g and j for 6 and 10 nm gaps, respectively. The features visualized in the photochemical near-field experiment showed very good agreement with the features in the electric field contour plots; the hotspot was localized along the edges of the prisms for all gap sizes for both experiment and simulation. The excitation mode visualized in this experiment is one of limited interest; the absorption band of the photosensitive polymer ends at around 600 nm. Currently, work is ongoing to explore options, such as two-photon absorption of the photopolymer, for visualizing the near-field features of modes excited by different wavelengths, especially those shown in Figure 3c.

The engineering of hotspots and surface plasmon localization are of interest for applications in SERS biosensing. The more localized an electric field hotspot is, the more intense it is, and thus, it will give more surface enhancement effects to Raman scattering signals. These enhanced signals allow for more sensitive detection of biomarkers. The effect of gap on electric

field enhancement was studied through Raman spectroscopy and DDA calculations on bowtie nanoantennae with gaps between prisms varying from 4 to 30 nm. Smaller gap sizes resulted in higher Raman enhancement for parallel polarization, while perpendicular polarization did not show significant change, as shown in Figure 3a. Polarizations parallel to the bowtie axis had higher enhancement factors than perpendicular polarization, shown in Figure 3b. The theoretical electric field enhancement was calculated with the use of electric field simulations in DDSCAT using 785 nm excitation, shown in Figure 3c. The electric field contour plot simulations for 785 nm excitation show that the hotspot is located in between the prisms for polarization parallel to the bowtie axis and on the outer corners for polarization perpendicular to the bowtie axis. The calculated electric field enhancement increases with decreasing gap size for polarization parallel to the bowtie axis, until the limit of the fabrication abilities, which agrees with simulation results and previous studies.<sup>17</sup> The Raman signal was not significantly enhanced by the polarization perpendicular to the antenna axis and did not vary significantly with changing gap size.

The electric field was simulated and experimentally explored using SERS and DDA electric field calculations for bowtie nanoantennae with varying prism sizes. An excitation wavelength of 785 nm was used for all simulations and experimental measurements. The prism size was varied from 120 to 180 nm for gap spacings from 4 to 30 nm. The electric field intensity increased with decreasing gap for all prism sizes in both experiment and simulation, as shown in Figure 3d and e, respectively. The calculated electric field peaked for prisms with a 140 nm side length and a 4 nm gap. The Raman enhancement factor was highest for the 160 nm prism size and 4 nm gap. The discrepancy between simulation and experiment for optimal prism size for 785 nm excitation may be due to the improved prism shape and corner sharpness that result from larger prism fabrication. If so, then improvements in fabrication technique may improve the experimental enhancement of the smaller prisms, and the data might more closely follow the trend predicted in simulation. It is noteworthy that 785 nm excitation is off-resonance, in varying degrees for different geometries. It would be of interest to explore on-resonance excitations in order to more carefully study the plasmon modes and fully exploit the potential of bowtie antennae as a SERS biosensing substrate.

It was of interest to observe the effect of the ROC of the corners of the prisms of a bowtie nanoantenna on optical properties and the electric field. By holding all other geometrical parameters constant and varying the fabrication recipe, specifically increasing the dosage of the electron beam, the ROC was controlled, and its effects on the electrical and optical properties were observed. The optical transmission spectra were taken of bowtie nanoantennae with both sharp and rounded corners for varying gap spacing between prisms. Both modes, due to polarization perpendicular and parallel to the bowtie axis, red shifted for increasing sharpness of the prism corners. Raman spectra were taken for bowtie nanoantennae with varying ROCs and gap sizes. The Raman enhancement factor increased with decreasing gap size for both round and sharp bowties, but the increase was more dramatic for the sharp bowties, as shown in Figure 3f. This agrees with the school of thought that electrons are more fully confined in the smaller ROC corners and would induce more electric field enhancement. It would be of interest to observe more ROCs through

controlled fabrication, ranging from circular dimers to prism dimers.

In this work, we have fabricated and characterized bowtie nanoantennae with varying gaps, prism sizes, and ROCs. We have been able to fabricate very small gaps in bowtie nanoantennae, in the sub-5 nm range, and have confirmed the continuation of trends found in previous work. The results on the variation of the bowtie prism size were found to agree with the studies on varying the size of individual prisms. We have found evidence that the ROC has a significant impact on the LSPR and electric field enhancement. We found that simulated predictions of the effects of geometry can be experimentally confirmed for the effect of gap and prism size on the SPR and the EF enhancement. The SPR peak corresponding to the parallel polarization was found to red shift with decreasing gap size while the peak corresponding to the perpendicular polarization remained fixed. The Raman signal enhancement was found to increase with decreasing gap for parallel polarization but did not change significantly for perpendicular polarization. The two modes, for polarization perpendicular and parallel to the bowtie axis, red shifted for increasing prism size. The trend of increasing enhancement with decreasing gap size was true for all prism sizes. As the ROC decreases and the prism corners become sharper, both resonance peaks red shift, and the Raman signal enhancement increases. This implies that the electric field enhancement is higher for sharper cornered bowties. The increased enhancement resulting from the decreasing gap sizes and ROC can be exploited for making highly sensitive biosensors.

Simulation of the particle scattering was carried out using the DDA in the DDSCAT program.<sup>27,28</sup> DDSCAT version 7.0 and a 1 nm grid were used for all simulations. The dielectric constants of Au are from Johnson and Christy.<sup>29</sup> The electric field intensity and thus the average and maximum intensity over the nanoparticle surface were calculated for isolated targets in an effective medium of refractive index 1.331. The information was used to make contour plots of the intensity on and around the nanoparticle to visualize the location of the hotspots. The extinction efficiency was simulated for multiple wavelengths to produce spectra used to determine the resonance position of the particle.

Electron beam lithography (EBL) was used to fabricate the bowtie nanoantenna arrays. The same polymer layer was used for all chips, 950 poly(methylmethacrylate) (PMMA) A4. The PMMA was spin coated onto the chips at 4000 rpm for 40 s (Specialty Coating Model P6700) and then baked at 180 °C for 15 min. EBL was performed using a JEOL JSM-7001F field emission scanning electron microscopy (FESEM) equipped with a Deben Beam Blanker and a nanometer pattern generation system (NPGS). After e-beam writing, the chips were developed for 75 s in a solution of 1:3-methyl isobutyl ketone (MIBK)/isopropyl alcohol (IPA) at room temperature. After development, the chips were rinsed for 20 s in IPA and blown dry using nitrogen or compressed air. Evaporation of 2 nm Cr and 30 nm Au was sequentially done in a thermal evaporator (Elite Engineering, Singapore). The chamber pressure of  $2 \times 10^{-7}$  Torr and evaporation rate of 0.6 Å/s were used for evaporation. Liftoff was done at room temperature in acetone for 2 h followed by a sonication for 1–2 min at a power level of 2 (Crest Ultrasonics Powersonic P1100D).

Bowtie geometry was confirmed by analysis in SEM; an example is shown in Figure 1a. Also shown in Figure 1a is a

illustration demonstrating the geometrical parameters defined as the prism side length,  $l$ , thickness,  $t$ , and gap between prisms,  $\delta$ . Statistical analysis was done for the gap size and prism size at 30 000 $\times$  magnification for 36 bowties per sample and was confirmed at 120 000 $\times$  magnification for each sample. The nominally 5, 10, 15, 20, 25, and 30 nm gaps had actual gaps of  $5.5 \pm 1.5$ ,  $10.8 \pm 1.9$ ,  $12.1 \pm 3.2$ ,  $20.3 \pm 1.1$ ,  $26.1 \pm 1.3$ , and  $29.6 \pm 1.5$  nm, respectively. The nominal prism side lengths of 180, 160, 140, and 120 nm had actual lengths of  $179.8 \pm 4.0$ ,  $158.1 \pm 3.7$ ,  $139.9 \pm 3.8$ , and  $108.8 \pm 3.3$  nm, respectively. The sharp and round bowties had tip ROCs of  $16.6 \pm 2.8$  and  $28.8 \pm 2.0$  nm, respectively. Round bowties had nominal gaps of 5, 10, 15, 20, and 25 nm and actual gaps of  $5.4 \pm 2.0$ ,  $9.9 \pm 1.6$ ,  $16.9 \pm 2.5$ ,  $19.6 \pm 1.1$ , and  $24.1 \pm 2.3$  nm, respectively.

Transmission spectroscopy on a microspectrophotometer (Craic, U.S.A.) with nonpolarized light in air, with an angle of incidence of 90° and an aperture size 15  $\mu$ m, was performed for three locations per sample. Each sampling measured around 225 bowties.

The molecule used for SERS experiments was 2-naphthalenethiol from Sigma-Aldrich. Substrates were incubated at room temperature in a solution of methanol with a concentration of 5 mM naphthalenethiol for 24 h and then rinsed with methanol and blown dry with nitrogen gas. Raman spectroscopy was conducted with a 785 nm excitation wavelength and a power of 2 mW. A 50 $\times$  objective with a slit of 300  $\mu$ m and a numerical aperture of 0.75 was used, with an integration time of 600 s per sample; each sampling measured around 16 bowties. Three locations on each sample were tested for both polarizations, parallel and perpendicular to the antenna axis. The Raman enhancement factor is a quantitative measure of the increase in Raman signal due to the enhanced electric field in SERS substrates and is given by

$$EF = \left( \frac{N_{\text{bulk}}}{N_{\text{SERS}}} \right) \left( \frac{I_{\text{SERS}}}{I_{\text{bulk}}} \right)$$

where  $N_{\text{bulk}}$  is the total number of molecules in the bulk sample,  $N_{\text{SERS}}$  in this work is the number of molecules contributing to the SERS signal,  $I_{\text{bulk}}$  is the intensity of the Raman signal for the bulk sample, and  $I_{\text{SERS}}$  is the intensity of the Raman signal for the SERS sample. It should be noted that in this work, the  $N_{\text{SERS}}$  has been normalized for the volume of the hotspot as determined from DDA electric near-field contour plots and assuming a self-assembling monolayer of thiolated molecule on the surface of the gold. In this Letter, we used naphthalenethiol, which has a molecular footprint of 0.42 nm<sup>2</sup>.<sup>30</sup>

Photochemical near-field imaging was done using an approach similar to that reported by Haggui and co-workers.<sup>31</sup> A thin film of DR1/PMMA was spin-coated onto the substrate. AFM images were taken of polymer-coated nanoparticles. The sample was exposed at 568 nm using an Ar–Kr laser source, with a power of 200 mW/cm<sup>2</sup>, for 40 min. The polarization was along the major axis of the bowtie. AFM images were taken after exposure of the same nanoparticles. Differential images were obtained through postprocessing image subtraction.

## AUTHOR INFORMATION

### Corresponding Author

\*E-mail: jerome.plain@utt.fr (J.P.); lizs@ntu.edu.sg (S.L.); qihua@ntu.edu.sg (Q.X.).

### Notes

The authors declare no competing financial interest.

## ACKNOWLEDGMENTS

The author Q.X. would like to acknowledge the strong support from the Singapore National Research Foundation through a Fellowship Grant (NRF-RF2009-06) and start-up grant support from Nanyang Technological University (M58110061). Q.X. and S.L. gratefully acknowledge the strong support from the Singapore Ministry of Education via two Tier 2 Grants (MOE2011-T2-2-051 and MOE2011-T2-2-085), respectively. The author J.P. would like to acknowledge the financial support of Nano'Mat ([www.nanomat.eu](http://www.nanomat.eu)) by the Ministère de l'enseignement supérieur et de la recherche, the Conseil régional Champagne-Ardenne, the FEDER funds, and the Conseil général de l'Aube. Q.X., S.L.D., and J.P. would like to acknowledge the France–Singapore Merlion Project.

## REFERENCES

- (1) Halas, N. J.; Lal, S.; Link, S.; Chang, W. S.; Natelson, D.; Hafner, J. H.; Nordlander, P. A Plethora of Plasmonics from the Laboratory for Nanophotonics at Rice University. *Adv. Mater.* **2012**, *24*, 4842–4877.
- (2) Wulfschlegel, J. D.; Liotta, L. A.; Petricoin, E. F. Proteomic Applications for the Early Detection of Cancer. *Nat. Rev. Cancer* **2003**, *3*, 267–275.
- (3) Anker, J. N.; Hall, W. P.; Lyandres, O.; Shah, N. C.; Zhao, J.; Van Duyne, R. P. Biosensing with Plasmonic Nanosensors. *Nat. Mater.* **2008**, *7*, 442–453.
- (4) Moskovits, M. Surface-Enhanced Spectroscopy. *Rev. Mod. Phys.* **1985**, *57*, 783–826.
- (5) Halas, N. J.; Lal, S.; Chang, W. S.; Link, S.; Nordlander, P. Plasmons in Strongly Coupled Metallic Nanostructures. *Chem. Rev.* **2011**, *111*, 3913–3961.
- (6) Fleischmann, M.; Hendra, P. J.; McQuillan, A. J. Raman-Spectra of Pyridine Adsorbed at a Silver Electrode. *Chem. Phys. Lett.* **1974**, *26*, 163–166.
- (7) Miller, S. K.; Baiker, A.; Meier, M.; Wokaun, A. Surface-Enhanced Raman-Scattering and the Preparation of Copper Substrates for Catalytic Studies. *J. Chem. Soc., Faraday Trans. 1* **1984**, *80*, 1305–1312.
- (8) Davies, J. P.; Pachuta, S. J.; Cooks, R. G.; Weaver, M. J. Surface-Enhanced Raman-Scattering from Sputter-Deposited Silver Surfaces. *Anal. Chem.* **1986**, *58*, 1290–1294.
- (9) Kneipp, K.; Wang, Y.; Kneipp, H.; Perelman, L. T.; Itzkan, I.; Dasari, R.; Feld, M. S. Single Molecule Detection Using Surface-Enhanced Raman Scattering (SERS). *Phys. Rev. Lett.* **1997**, *78*, 1667–1670.
- (10) Xu, H. X.; Bjerneld, E. J.; Kall, M.; Borjesson, L. Spectroscopy of Single Hemoglobin Molecules by Surface Enhanced Raman Scattering. *Phys. Rev. Lett.* **1999**, *83*, 4357–4360.
- (11) Jensen, T. R.; Schatz, G. C.; Van Duyne, R. P. Nanosphere Lithography: Surface Plasmon Resonance Spectrum of a Periodic Array of Silver Nanoparticles by Ultraviolet-Visible Extinction Spectroscopy and Electrodynamic Modeling. *J. Phys. Chem. B* **1999**, *103*, 2394–2401.
- (12) Kahl, M.; Voges, E.; Kostrewa, S.; Viets, C.; Hill, W. Periodically Structured Metallic Substrates for SERS. *Sens. Actuators, B* **1998**, *51*, 285–291.
- (13) Koh, A. L.; Fernandez-Dominguez, A. I.; McComb, D. W.; Maier, S. A.; Yang, J. K. W. High-Resolution Mapping of Electron-Beam-Excited Plasmon Modes in Lithographically Defined Gold Nanostructures. *Nano Lett.* **2011**, *11*, 1323–1330.
- (14) Kelly, K. L.; Coronado, E.; Zhao, L. L.; Schatz, G. C. The Optical Properties of Metal Nanoparticles: The Influence of Size, Shape, and Dielectric Environment. *J. Phys. Chem. B* **2003**, *107*, 668–677.
- (15) Chu, Y. Z.; Banaee, M. G.; Crozier, K. B. Double-Resonance Plasmon Substrates for Surface-Enhanced Raman Scattering with Enhancement at Excitation and Stokes Frequencies. *ACS Nano* **2010**, *4*, 2804–2810.
- (16) Zhu, W. Q.; Banaee, M. G.; Wang, D. X.; Chu, Y. Z.; Crozier, K. B. Lithographically Fabricated Optical Antennas with Gaps Well Below 10 nm. *Small* **2011**, *7*, 1761–1766.
- (17) Hao, E.; Schatz, G. C. Electromagnetic Fields around Silver Nanoparticles and Dimers. *J. Chem. Phys.* **2004**, *120*, 357–366.
- (18) Hubert, C.; Bachelot, R.; Plain, J.; Kostcheev, S.; Lerondel, G.; Juan, M.; Royer, P.; Zou, S. L.; Schatz, G. C.; Wiederrecht, G. P.; Gray, S. K. Near-Field Polarization Effects in Molecular-Motion-Induced Photochemical Imaging. *J. Phys. Chem. C* **2008**, *112*, 4111–4116.
- (19) Juan, M. L.; Plain, J.; Bachelot, R.; Vial, A.; Royer, P.; Gray, S. K.; Montgomery, J. M.; Wiederrecht, G. P. Plasmonic Electromagnetic Hot Spots Temporally Addressed by Photoinduced Molecular Displacement. *J. Phys. Chem. A* **2009**, *113*, 4647–4651.
- (20) Fromm, D. P.; Sundaramurthy, A.; Schuck, P. J.; Kino, G.; Moerner, W. E. Gap-Dependent Optical Coupling of Single “Bowtie” Nanoantennas Resonant in the Visible. *Nano Lett.* **2004**, *4*, 957–961.
- (21) Tabor, C.; Murali, R.; Mahmoud, M.; El-Sayed, M. A. On the Use of Plasmonic Nanoparticle Pairs As a Plasmon Ruler: The Dependence of the Near-Field Dipole Plasmon Coupling on Nanoparticle Size and Shape. *J. Phys. Chem. A* **2009**, *113*, 1946–1953.
- (22) Hatab, N. A.; Hsueh, C. H.; Gaddis, A. L.; Retterer, S. T.; Li, J. H.; Eres, G.; Zhang, Z. Y.; Gu, B. H. Free-Standing Optical Gold Bowtie Nanoantenna with Variable Gap Size for Enhanced Raman Spectroscopy. *Nano Lett.* **2010**, *10*, 4952–4955.
- (23) Duan, H. G.; Fernandez-Dominguez, A. I.; Bosman, M.; Maier, S. A.; Yang, J. K. W. Nanoplasmonics: Classical down to the Nanometer Scale. *Nano Lett.* **2012**, *12*, 1683–1689.
- (24) Ding, W.; Bachelot, R.; Kostcheev, S.; Royer, P.; de Lamaestre, R. E. Surface Plasmon Resonances in Silver Bowtie Nanoantennas with Varied Bow Angles. *J. Appl. Phys.* **2010**, *108*, 124314–124320.
- (25) Rechberger, W.; Hohenau, A.; Leitner, A.; Krenn, J. R.; Lamprecht, B.; Aussenegg, F. R. Optical Properties of Two Interacting Gold Nanoparticles. *Opt. Commun.* **2003**, *220*, 137–141.
- (26) Guiton, B. S.; Iberi, V.; Li, S. Z.; Leonard, D. N.; Parish, C. M.; Kotula, P. G.; Varela, M.; Schatz, G. C.; Pennycook, S. J.; Camden, J. P. Correlated Optical Measurements and Plasmon Mapping of Silver Nanorods. *Nano Lett.* **2011**, *11*, 3482–3488.
- (27) Draine, B. T.; Flatau, P. J. Discrete-Dipole Approximation for Scattering Calculations. *J. Opt. Soc. Am. A* **1994**, *11*, 1491–1499.
- (28) Draine, B. T.; Flatau, P. J. Discrete-Dipole Approximation for Periodic Targets: Theory and Tests. *J. Opt. Soc. Am. A* **2008**, *25*, 2693–2703.
- (29) Johnson, P. B.; Christy, R. W. Optical Constants of Noble Metals. *Phys. Rev. B* **1972**, *6*, 4370–4379.
- (30) Kolega, R. R.; Schlenoff, J. B. Self-Assembled Monolayers of an Aryl Thiol: Formation, Stability, and Exchange of Adsorbed 2-Naphthalenethiol and Bis(2-naphthyl) Disulfide on Au. *Langmuir* **1998**, *14*, 5469–5478.
- (31) Haggui, M.; Dridi, M.; Plain, J.; Marguet, S.; Perez, H.; Schatz, G. C.; Wiederrecht, G. P.; Gray, S. K.; Bachelot, R. Spatial Confinement of Electromagnetic Hot and Cold Spots in Gold Nanocubes. *ACS Nano* **2012**, *6*, 1299–1307.